

BioVessel-Net and RetinaMix: Unsupervised Retinal Vessel Segmentation from OCTA Images

Cheng Huang^{1,2,3,+}, Weizheng Xie^{2,4,+}, Fan Gao¹, Yutong Liu¹, Ruoling Wu^{1,5}, Zeyu Han^{2,6}, Jingxi Qiu⁶, Xiangxiang Wang^{1,†}, Zhenglin Yang^{1,7,†}, Hao Wang^{1,8}, and Yongbin Yu^{1,†}

¹University of Electronic Science and Technology of China, Chengdu, 610056, China

²Southern Methodist University, Dallas, 75205, USA

³University of Texas Southwestern Medical Center, Dallas, 75390, USA

⁴Karat by Lollicup, Rockwall, 75032, USA

⁵University Medical Center Utrecht, Utrecht, 3584 CX, The Netherlands

⁶Georgetown University, Washington, 20057, USA

⁷Sichuan Provincial People's Hospital, Chengdu, 610072, China

⁸University of Connecticut, Storrs, 06269, USA

†Corresponding Author: ybyu@uestc.edu.cn

+these authors contributed equally to this work

ABSTRACT

Structural changes in retinal blood vessels are critical biomarkers for the onset and progression of glaucoma and other ocular diseases. However, current vessel segmentation approaches largely rely on supervised learning and extensive manual annotations, which are costly, error-prone, and difficult to obtain in optical coherence tomography angiography. Here we present BioVessel-Net, an unsupervised generative framework that integrates vessel biostatistics with adversarial refinement and a radius-guided segmentation strategy. Unlike pixel-based methods, BioVessel-Net directly models vascular structures with biostatistical coherence, achieving accurate and explainable vessel extraction without labeled data or high-performance computing. To support training and evaluation, we introduce RetinaMix, a new benchmark dataset of 2D and 3D OCTA images with high-resolution vessel details from diverse populations. Experimental results demonstrate that BioVessel-Net achieves near-perfect segmentation accuracy across RetinaMix and existing datasets, substantially outperforming state-of-the-art supervised and semi-supervised methods. Together, BioVessel-Net and RetinaMix provide a label-free, computationally efficient, and clinically interpretable solution for retinal vessel analysis, with broad potential for glaucoma monitoring, blood flow modeling, and progression prediction. Code and dataset are available: <https://github.com/VikiXie/SatMar8>.

Introduction

Glaucoma is a leading cause of irreversible blindness, often progressing silently until substantial vision loss has occurred^{1,2}. Recent evidence suggests that choroidal microvasculature dropout may serve as a potential biomarker for disease progression³. Optical Coherence Tomography Angiography (OCTA) enables non-invasive, depth-resolved visualization of these vascular alterations, yet reliable quantification of choroidal vessel density remains a significant challenge^{4,5}.

Current imaging analytics for glaucoma primarily rely on computer vision techniques⁶⁻¹⁴. In particular, supervised learning segmentation models (SLSMs)¹⁵⁻²³ have become widely used. However, SLSMs are often ill-suited for choroidal vessel analysis in OCTA due to their strong dependence on large annotated datasets^{24,25}, which are extremely difficult to obtain. The complex morphology of OCTA images, including irregular vessel patterns, dense and intersecting capillary networks, and the presence of large vessels that must be excluded, further complicates manual labeling and automated segmentation⁴.

Emerging studies have shown that retinal blood vessels follow biostatistical laws^{26,27}, where vessel radius variations along branching structures suggest that segmentation can bypass purely pixel-based mapping by leveraging radius as a discriminative feature²⁸⁻³¹. Motivated by this observation, we propose BioVessel-Net, an unsupervised framework that integrates generative adversarial networks with retinal vessel biostatistics to achieve precise main-vessel segmentation from OCTA images without requiring labeled data. To further address data scarcity, we introduce RetinaMix, a benchmark dataset of high-resolution 2D and 3D OCTA images with clear capillary distribution, supporting vessel segmentation, 3D reconstruction, and blood flow analysis.

This paper substantially extends our preliminary work presented at ICONIP 2025 (oral presentation; acceptance rate 6%), where we first introduced the X-GAN framework for unsupervised main-vessel segmentation⁵. In this journal version, we present BioVessel-Net, which incorporates vessel biostatistical priors to enhance clinical interpretability. We further contribute

RetinaMix, a curated dataset with demographic diversity, and conduct comprehensive evaluations including cross-dataset validation, ablation and sensitivity analyses, and efficiency benchmarking. These extensions transform the prototype into a clinically generalizable system with strong reproducibility, aligning with the translational scope of *Scientific Reports*.

This paper makes the following major contributions:

- We propose the BioVessel-Net, a biostatistics-guided unsupervised framework for retinal vessel analysis, which integrates vascular radius priors into a GAN-enhanced DFS segmentation pipeline. This design achieves near-perfect accuracy while maintaining strong biological interpretability.
- We construct and release the RetinaMix, a new high-resolution 2D/3D OCTA dataset comprising 550 images from 250 subjects, with balanced demographic representation across gender and race. This dataset provides an open benchmark for vessel structure analysis and glaucoma screening.
- We perform comprehensive evaluations across multiple datasets (RetinaMix, OCTA-500⁴, ROSE³²), including cross-dataset generalization, hyperparameter sensitivity, ablation studies, and efficiency analysis against SOTA supervised models. Results demonstrate both superior accuracy and computational efficiency.
- We demonstrate that the proposed threshold choice ($R_{min} \approx 0.2$) is consistent with independent ophthalmological findings on capillary coverage (≈ 18 -26%), thereby validating the biological plausibility of our approach and reinforcing its potential for clinical translation.

Related Work

Public Resources for Glaucoma Research

Glaucoma-related research has benefited from a wide range of publicly available fundus photograph datasets. Among the most frequently used are Drishti-GS³³ with 101 color fundus images that include expert annotations of the optic disc and cup, ORIGA³⁴ with 650 images that provide optic nerve head labels and cup-to-disc ratio measurements, and RIM-ONE³⁵ with 169 images collected from normal, glaucoma, and ocular hypertension cases. Population-based resources such as the Singapore Chinese Eye Study³⁶, which involves more than 3,300 subjects with comprehensive clinical annotations, offer additional large-scale epidemiological support. More recent contributions include MURED³⁷ with 2208 images and ROSE³² with 229 images, both of which provide curated fundus photographs with detailed labels for glaucoma assessment. Classic benchmarks for vessel segmentation such as DRIVE³⁸ with 40 images and STARE³⁹ with 20 images are often combined with glaucoma datasets to evaluate vascular biomarkers that are relevant to disease progression.

In addition to fundus photographs, OCTA-based datasets have become important for capturing microvascular changes associated with glaucoma. Notable examples include OCTA-500⁴, which contains imaging from 500 subjects, and the large-scale Harvard datasets, namely Harvard-GDP⁴⁰ with 21,059 samples and Harvard-GF⁴¹ with 3300 samples, which provide optical coherence tomography angiography linked to glaucoma phenotypes. Beyond single-modality imaging, multimodal and fairness-oriented datasets have also been introduced. FairSeg² and FairDomain¹ each contain 10,000 images or subjects, while FairCLIP²⁴ includes 10,000 samples and FairVision²⁵ includes 30,000 subjects. These collections integrate image data with textual corpora and support interdisciplinary developments at the interface of computer vision and natural language processing for ophthalmic research.

Medical Imaging for Glaucoma

In glaucoma research, medical imaging plays a central role in developing and validating automated diagnostic methods^{2,6,9,25,40}. Even when sufficient data are available, challenges remain in labeling quality and consistency, since subjective variability among clinicians may introduce biases and limit model performance⁴². Generative artificial intelligence (G-AI) provides a promising strategy to address data deficiencies and labeling inconsistencies, although human verification is still necessary and synthetic data may encounter similar annotation challenges^{14,43-47}. Among generative approaches, generative adversarial networks^{13,14,43,48} have been particularly influential because of their ability to mitigate both data scarcity and labeling difficulties in an unsupervised manner. In practice, GAN-based segmentation pipelines are typically coupled with dedicated segmentation networks. For this segmentor component, pre-trained architectures such as convolutional neural networks^{6,7,9}, U-Net¹⁵ and its variants^{16,17,49}, vision transformers^{10,50}, Mask R-CNN¹⁸, and more recently medical foundation models like MedSAM¹⁹ are frequently adopted to produce the final segmentation output. Recent work across both computer vision and medical imaging communities has consistently demonstrated the effectiveness of this paradigm for glaucoma-related imaging tasks.

Methodology

The complete framework of BioVessel-Net is illustrated in Figure 1 where red indicates that BioVessel-Net does not utilize these things in Segmentor S , whereas G-AI+SLSMS do. and it consists of two parts: *Vessel Structure Refinement Module* and *Segmentor*.

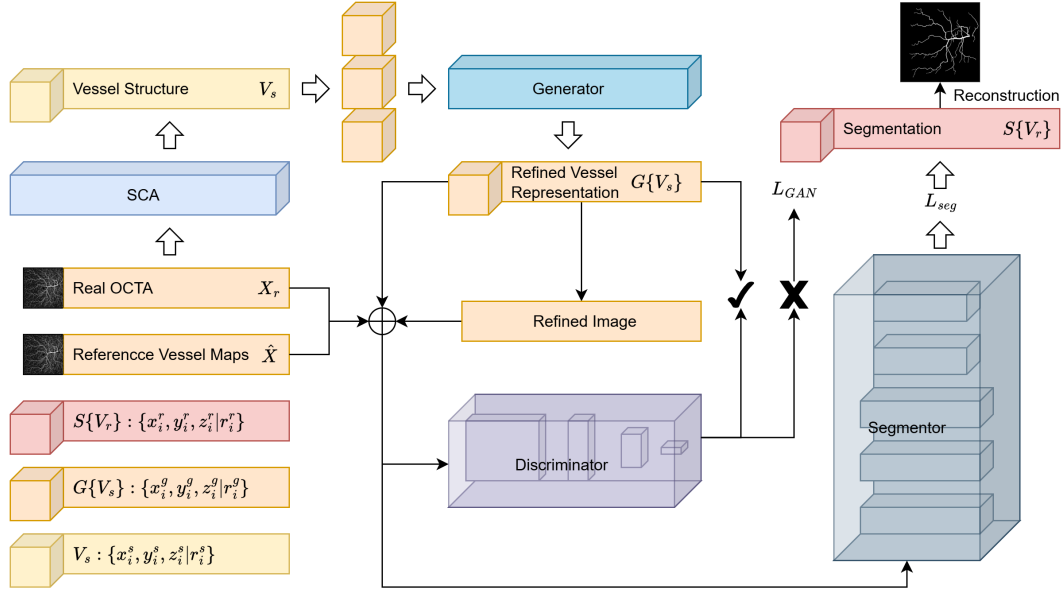


Figure 1. The Architecture of BioVessel-Net

Vessel Structure Refinement Module

In OCTA imaging, retinal blood vessels exhibit a uniform color change and have a shape closely resembling a path. They can be represented using coordinates along with road width. Space Colonization Algorithm (SCA)⁵¹ just meets this requirement. Rather than generating pixel-wise vessel segmentations, we formulate the vascular network as a structured graph representation, ensuring topological consistency and robust connectivity. The graph consists of the following components, shown in Equation 1:

$$V = \{(x_i, y_i, z_i | r_i)\}_{i=1}^N \quad (1)$$

where (x_i, y_i, z_i) are the spatial coordinates of the vessel centerline points, r_i represents the local vessel radius and N means the number of nodes. Given a vessel structure V_s via SCA, our generator G learns to transform it into a realistic OCTA-like representation V_r' , expressed as $G(V_s)$, while V_r' undergoes style adaptation to align with the contrast and noise characteristics of real OCTA images V_r . To enhance structural consistency, we modify the original CycleGAN architecture by removing the inverse generator and incorporating a segmentation consistency loss via the segmentor S . This modification prevents CycleGAN from altering the vessel topology, ensuring that vessel segmentation remains biologically meaningful, as illustrated in Equation 2:

$$L_{\text{seg}} = \mathbb{E}_{V_r} [\|S(V_r') - S(V_r)\|_1] \quad (2)$$

where $S(V)$ extracts vessel masks from OCTA images, enforcing structural consistency during transformation. This constraint ensures that CycleGAN adapts contrast while strictly preserving vessel topology. Consequently, our total loss function is formulated as follows:

$$L_{\text{GAN}} = \mathbb{E}_{V_r} [D(V_r)] - \mathbb{E}_{V_s} [D(G(V_s))] \quad (3)$$

$$L_{\text{GP}} = \lambda \mathbb{E}_{\hat{V}} [\left(\|\nabla_{\hat{V}} D(\hat{V})\|_2 - 1\right)^2] \quad (4)$$

$$L_{\text{total}} = L_{\text{GAN}} + \lambda_{\text{GP}} L_{\text{GP}} + \lambda_{\text{seg}} L_{\text{seg}} \quad (5)$$

where Equation 3 is the Wasserstein Adversarial Loss, Equation 4 is the Gradient Penalty for Stability (\hat{X} is the reference vessel representation) and Equation 5 is the Structural Consistency via Segmentation Loss. Upon training convergence, the generator produces a vessel structure that not only exhibits realistic contrast properties but also preserves anatomical coherence, ensuring fidelity to real OCTA characteristics.

Segmentor

Rather than utilizing pixel-wise segmentation maps, we directly extract primary vessels from the $(x_i^G, y_i^G, z_i^G | r_i^G)$ representation using DFS based graph traversal⁵², which effectively isolates large vessels while filtering out capillaries.

First, we construct a graph $G = (V, E)$, where nodes V represent vessel centerline points and edges E connect adjacent vessel points based on local vessel connectivity. A vessel segment e_{ij} between nodes v_i and v_j (the direction is from i to j) is assigned a weight, as shown in Equation 6:

$$w(e_{ij}) = r_i \quad (6)$$

where larger vessels are prioritized in the traversal process. To extract primary vessels, we apply radius thresholding and DFS traversal⁵². For radius filtering, we define a minimum main vessel radius R_{min} and retain only Equation 7:

$$V_{main} = \{(x_i, y_i, z_i | r_i) \mid r_i \geq (R_{min} * r_{max})\} \quad (7)$$

For DFS traversal, it consists of three steps:

- select the optic disc region as the root node
- recursively traverse the largest connected component using DFS
- stop when no further vessel segments satisfy the radius constraint

when all three steps finished, construct final extracted vessel structure G_{main} . This approach effectively retains only the primary vascular structure, removing small capillaries and noise. This method can be summarized as the following Algorithm 1.

Algorithm 1 Primary Vessel Extraction via DFS

Require: Vessel Structure $V = \{(x_i, y_i, z_i | r_i)\}_{i=1}^N$

Ensure: Extracted Primary Vessel Graph G_{main}

- 1: **Step 1: Vessel Graph Construction**
 - 2: **for all** vessel point $(x_i, y_i, z_i | r_i) \in V$ **do**
 - 3: Identify Neighboring Vessel Points to Form Edge Set E
 - 4: Assign Edge Weight $w(e_{ij}) = r_i$
 - 5: **end for**
 - 6: **Step 2: Vessel Filtering**
 - 7: Apply Radius Threshold R_{min}
 - 8: $V_{main} = \{(x_i, y_i, z_i | r_i) \mid r_i \geq R_{min} \cdot r_{max}\}$
 - 9: Remove Weakly Connected Components
 - 10: **Step 3: DFS-Based Traversal**
 - 11: Initialize DFS from Optic Disc Region
 - 12: **for all** point $(x_i, y_i, z_i | r_i) \in V_{main}$ **do**
 - 13: Recursively Explore Vessel Network via DFS
 - 14: Preferentially Expand along Thicker Vessels
 - 15: **end for**
 - 16: **Step 4: Output**
 - 17: **return** G_{main}
-

As shown in Figure 2, the key aspect of Algorithm 1 is the threshold R_{min} . Instead of only examining the final image, we analyze intermediate outputs, CSV-derived statistics, and GAN-generated vessel radius distributions. For a representative image, we computed a Mean of 85.31 and a Standard Deviation of 88.67, which determined R_{min} as $0.1968 r_{max}$. Across the datasets, the corresponding values were 0.2011 (RetinaMix), 0.2102 (OCTA-500), and 0.1982 (ROSE). For consistency, R_{min} was standardized to 0.2. Independent ophthalmology analyses confirm that OCTA images typically exhibit 18-26% capillary coverage, supporting the validity of this threshold.

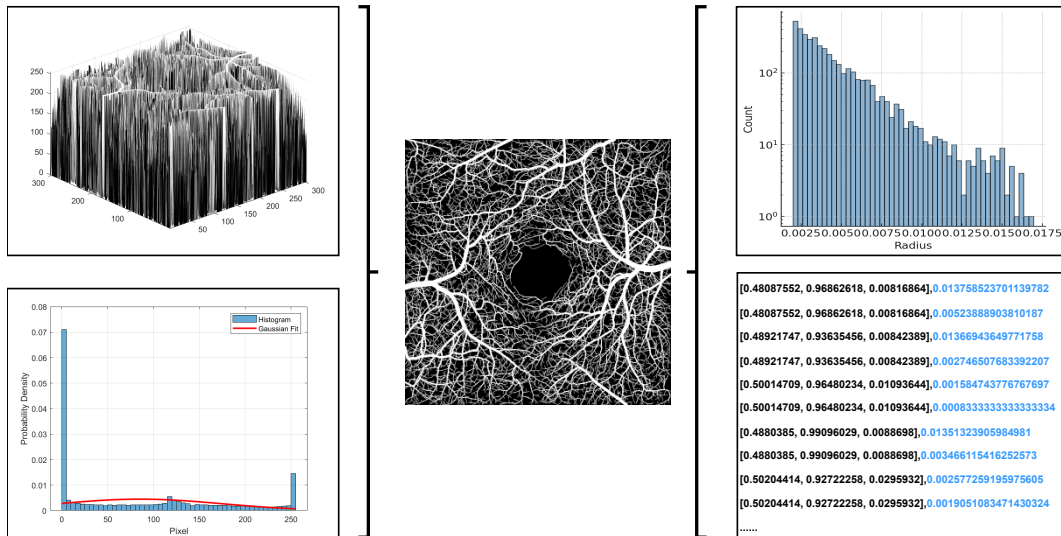


Figure 2. Details of One Sample: 3D Visualization, Statistical Distribution, Radius Statistics and Vascular Data

Dataset & Implementation

Dataset

OCTA-500

The OCTA-500⁴ is a large-scale retinal OCTA resource comprising 500 en face images acquired under two scanning protocols: a wide-field 6 mm × 6 mm view (300 images, ID 10001-10300) for global vascular assessment and a high-resolution 3 mm × 3 mm view (200 images, ID 10301-10500) for detailed fovea-centered microvascular analysis. Each image is accompanied by expert annotations that delineate arteries, veins, large vessels, capillaries, and both two-dimensional and three-dimensional foveal avascular zones (FAZ), providing comprehensive ground truth for vascular morphology studies. With its dual-scale design, OCTA-500 supports both wide-field examination of retinal circulation and fine-grained investigation of capillary networks, offering a standardized benchmark for vessel segmentation, classification, and FAZ analysis in the study of retinal structure and disease progression.

ROSE

The ROSE³² is the first publicly available benchmark dedicated to vessel segmentation in OCTA images. It comprises 229 images with expert manual annotations at either pixel or centerline level. The dataset includes two subsets: ROSE-1, containing 117 images from 39 subjects (26 with Alzheimer’s disease and 13 healthy controls) with both pixel-level and centerline annotations; and ROSE-2, consisting of 112 images from 112 eyes with macular diseases, annotated at the centerline level. The images were captured using two different OCTA systems (Optovue RTVue XR Avanti and Heidelberg OCT2), both covering a 3 × 3 mm² fovea-centered region. ROSE provides a standardized resource for training and evaluating OCTA vessel segmentation methods and has been applied to investigate retinal microvascular biomarkers in neurodegenerative diseases.

RetinaMix

RetinaMix is a unique and pioneering dataset focused exclusively on retinal vascularity. The dataset features an exceptionally clear distribution of capillaries. It comprises 550 images, both 2D and 3D, from 250 subjects, ensuring fair representation across gender and race. We collected retinal vascular data for both eyes (OS and OD) of each subject, with a gender split of 48.8% male and 51.2% female. Racial distribution reflects local glaucoma clinic demographics: 80.4% white, 14.6% Black, with Asians and other minority groups comprising the remainder. Additional data includes age (47.1 ± 24.8 years) and examination dates from 2023 to 2024. RetinaMix’s original images come from the latest Intalight device¹, offering superior detail compared to OPTOVUE² (Figure 3). As shown in Figure 3a and Figure 3c, Intalight images feature clearer vessel boundaries and capillary distributions, enhancing segmentation accuracy. In supervised learning, their minimal pixel variation introduces valuable noise for testing model robustness. For 3D reconstruction and evolution prediction, these high-resolution images aid in vascular modeling and blood flow analysis, making Intalight data ideal for both tasks.

¹<https://intalight.com/>

²<https://www.visionix.com/>

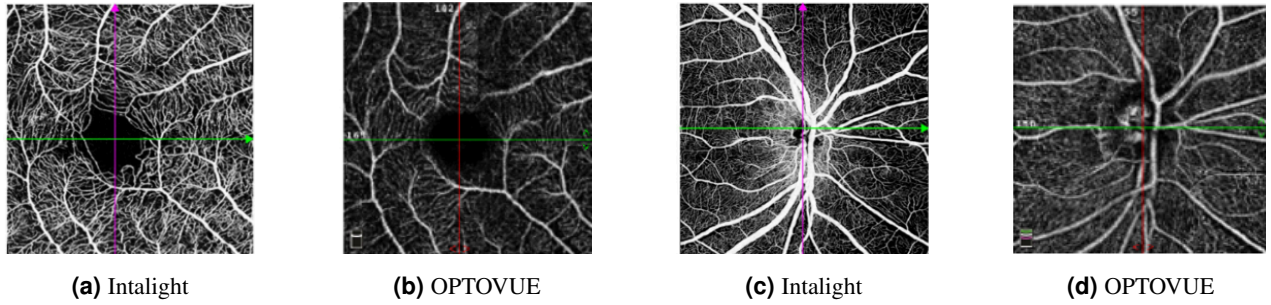


Figure 3. Comparison of Data Collected by Different Devices for the Same Patient

For RetinaMix, we eliminate red and green baselines from Intalight device images through a multi-step process. First, we apply a dark channel algorithm⁵³ to remove light artifacts, followed by unsharp masking⁵⁴ to enhance high-frequency details. The final images (Figure 4a) undergo manual verification for quality assurance. As shown in Figure 4, while main vessels remain visible across datasets, magnification reveals that OCTA-500⁴ and ROSE³² blur capillaries and vessel ends. Even the unprocessed baseline image (Figure 3b) offers superior vessel clarity compared to other datasets (Figure 4c, Figure 4b). Among them, Figure 3a and Figure 3b are images of deep angio, and Figure 3c and Figure 3d are images of superficial angio. They all are images of inner retina vessel.

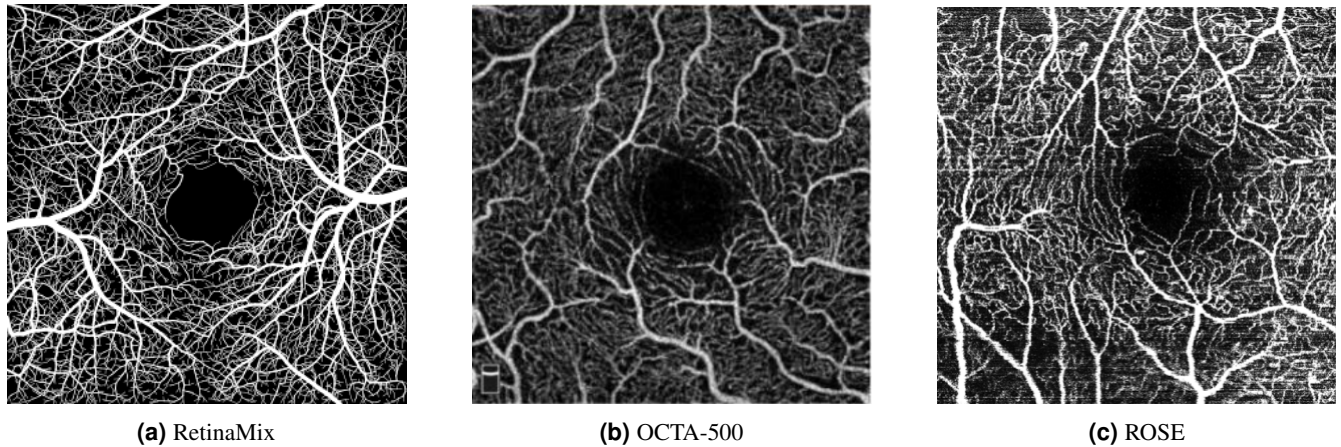


Figure 4. Comparison of RetinaMix with Other Datasets

For the representation of 3D imaging of RetinaMix, as shown in Figure 5, capillaries stand out from the thicker main blood vessels by attaching to them and narrowing at their ends (Figure 5c). The elaborate architecture of blood vessels and the intertwining capillaries contribute to an extremely intricate vascular layout. 3D imaging part of RetinaMix is formatted as a JSON file, which includes 3D X, Y, and Z coordinates and the corresponding radius pixel distribution values. For annotation (2D, image format: PNG), our team includes two glaucoma specialists who handle labeling, verification, and manual evaluation, utilizing the Labelme³.

In general, RetinaMix is a dataset that combines 2D and 3D images with extremely high image resolution, and is particularly dedicated to retinal vascular segmentation.

Implementation

Hyperparameter

For BioVessel-Net, its generator adopts a ResNet 9-block architecture⁵⁵, while the discriminator utilizes PatchGAN⁵⁶ (70×70). The optimizer is Adam⁵⁷ with a learning rate of 2×10^{-4} and momentum parameters $\beta_1 = 0.5$, $\beta_2 = 0.999$. BioVessel-Net is trained for 50 epochs, with a linear learning rate decay to 0 after 25 epochs, with evaluation performed using 10-fold cross-validation. Data augmentation includes: random rotations ($k \times 90^\circ \pm 10^\circ$), flipping and contrast adjustments.

³<https://github.com/wkentaro/labelme>

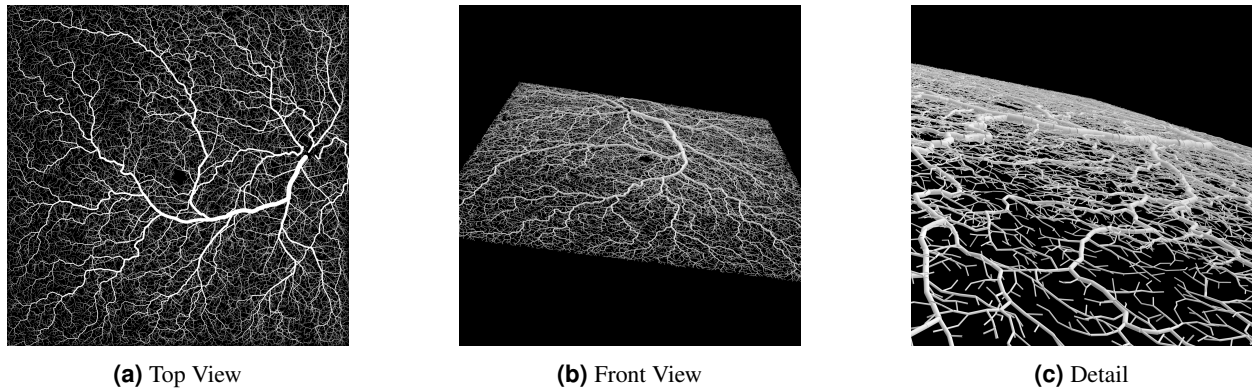


Figure 5. 3D Imaging of Retinal Vessel from Various Angles

Evaluation Metric

We use *Intersection over Union*⁵⁸ (IoU), also known as the *Jaccard Index*, to measure similarity between the predicted segmentation and the ground truth. This metric ranges from 0 to 1, with 1 indicating perfect segmentation. Additionally, we use the *Dice Coefficient*⁵⁹, another metric for segmentation accuracy that calculates overlap between the prediction and ground truth. All in all, IoU is used to evaluate segmentation accuracy of the main vessels, while the Dice Coefficient assesses accuracy at finer vessel ends relative to the main vessels. For vascular structural enhancement, we use the *Structural Similarity Index*⁶⁰ (SSIM) and the *Mean Squared Error*⁶¹ (MSE). SSIM (range: -1 to 1) assesses similarity based on luminance, contrast, and structure, while MSE quantifies pixel-wise differences, with lower values indicating higher similarity. While SSIM aligns with human perception, MSE focuses on absolute pixel differences.

Finally, the best results in each column are highlighted in bold, and the second-best results are indicated with underline.

Hardware

The hardware specifications for training and testing include 2 Tesla V100 GPUs ($2 \times 32\text{GB}$), 64GB of RAM, 8 CPU cores per node, and a total of 6 nodes.

Experimental Result

Baseline Model

All final experimental results are the average of ten cross-validation times. All selected models' hyperparameters have been optimized by Optuna⁴. Finally, we selected many SOTA models for experimental verification:

CNN-based Model

We included several classic convolutional neural network (CNN) architectures: U-Net¹⁵, U-Net++¹⁶, SegNet⁶², DeepLabV3+⁶³, Mask R-CNN¹⁸, and YOLOv11-x¹¹. These models represent widely adopted backbones for medical image segmentation tasks.

Transformer-based Model

To incorporate recent advances in transformer architectures, we evaluated TransUNet²¹, Attention U-Net¹⁷ and Swin-UNet²⁰, which combine self-attention mechanisms with encoder-decoder designs.

Large-scale Pretrained Model

We further benchmarked foundation models designed for general-purpose segmentation, including SAM⁶⁴ and its medical adaptation MedSAM¹⁹.

Self-supervised and Universal Framework

Representative frameworks in this category include CauSSL¹², UniverSeg⁶⁵, S2VNet⁶⁶, and Tyche⁶⁷, which leverage self-supervised or universal segmentation strategies to improve generalizability across domains.

G-AI based Method

We incorporated adversarial segmentation models such as SegAN⁴⁸, Vessel-GAN⁶⁸, LGGAN⁶⁹, CSGAN⁷⁰, CycleGAN-Seg⁷¹, CycleGAN¹⁴, and a generic GAN baseline¹³. These approaches use adversarial training to enhance boundary accuracy and robustness.

⁴<https://optuna.org/>

Ophthalmology-specific Model

Finally, we included OCTA-Net⁷², which is specifically designed for retinal and choroidal vessel segmentation in OCTA images.

Comparative Experiment

Benchmarking BioVessel-Net Against Competing Approaches

As shown in Table 1, across all datasets, BioVessel-Net consistently achieves the best performance, with IoU and Dice scores surpassing 99%. Particularly, on RetinaMix (6 mm), it records 99.41 IoU and 99.71 Dice, and on OCTA-500 (3 mm) it achieves 99.42 IoU and 99.71 Dice, markedly outperforming the strongest baselines such as MedSAM¹⁹ and OCTA-Net⁷². The improvement is more pronounced in cross-dataset generalization, where BioVessel-Net demonstrates superior robustness compared with both CNN-^{11,15,16,18,62,63} and transformer-based methods^{17,20,21}. These results highlight the effectiveness of incorporating biostatistical priors into a GAN-driven segmentation framework, yielding both high accuracy and strong generalizability.

Table 1. Comparison BioVessel-Net With Other Models on RetinaMix, OCTA-500 and ROSE ($\times 100\%$)

Model	Dataset									
	RetinaMix				OCTA-500				ROSE	
	6mm		3mm		6mm		3mm		3mm	
	IoU	Dice								
U-Net ¹⁵	95.14	97.51	95.23	97.56	96.93	98.44	98.75	99.37	97.94	98.96
U-Net++ ¹⁶	95.68	97.81	96.64	98.29	97.65	98.81	97.96	98.97	97.52	98.75
Attention U-Net ¹⁷	95.78	97.84	96.04	97.98	97.05	98.50	98.61	99.30	97.92	98.95
Mask R-CNN ¹⁸	92.35	96.02	91.35	95.48	92.06	95.87	93.50	96.64	91.23	95.41
YOLOv11-x ¹¹	95.81	97.86	96.55	98.24	95.93	97.92	97.66	98.82	97.83	98.89
MedSAM ¹⁹	96.38	98.16	96.47	98.20	96.01	97.95	98.94	99.47	97.89	98.93
CauSSL ¹²	95.23	97.56	95.47	97.68	96.32	98.04	98.15	99.08	97.80	98.89
UniverSeg ⁶⁵	95.30	97.58	95.52	97.70	96.58	98.17	98.42	99.22	97.07	98.01
S2VNet ⁶⁶	95.68	97.81	95.36	97.63	96.45	98.11	98.27	99.15	97.92	98.95
Tyche ⁶⁷	95.80	97.85	95.19	97.53	96.28	98.02	98.11	99.06	97.76	98.87
DeepLabV3+ ⁶³	95.72	97.68	95.38	97.62	96.21	98.05	97.82	98.95	97.55	98.81
SegNet ⁶²	95.30	97.41	95.02	97.25	95.84	97.96	97.40	98.72	97.21	98.56
TransUNet ²¹	96.42	98.09	96.13	98.00	97.11	98.44	98.23	99.07	97.86	98.92
Swin-UNet ²⁰	96.51	98.15	96.24	98.05	97.19	98.50	98.27	99.11	97.91	98.94
OCTA-Net ⁷²	96.68	98.23	96.39	98.12	97.35	98.58	98.32	99.13	97.94	98.96
SAM ⁶⁴	96.22	98.01	95.95	97.86	97.02	98.36	98.16	99.03	97.82	98.88
SegAN ⁴⁸	95.61	97.55	95.32	97.43	96.08	98.02	97.58	98.81	97.36	98.62
Vessel-GAN ⁶⁸	96.37	98.07	96.08	97.94	97.14	98.42	98.20	99.06	97.89	98.91
LGGAN ⁶⁹	95.74	97.66	95.45	97.53	96.25	98.09	97.69	98.87	97.48	98.71
CSGAN ⁷⁰	95.80	97.70	95.51	97.58	96.33	98.12	97.73	98.90	97.52	98.74
CycleGAN-Seg ⁷¹	95.91	97.75	95.63	97.64	96.41	98.18	97.79	98.92	97.59	98.77
BioVessel-Net	99.41	99.71	98.66	99.33	99.21	99.60	99.42	99.71	99.19	99.59

Evaluating Cross-Dataset Robustness of BioVessel-Net

Table 2 reports mixed validation results. When trained on RetinaMix and tested on OCTA-500, BioVessel-Net achieved 99.21 IoU and 99.60 Dice, higher than MedSAM¹⁹ (97.95/98.84), OCTA-Net⁷² (98.36/98.92), and Swin-UNet²⁰ (98.10/98.71). In the reverse setting (OCTA-500 \rightarrow RetinaMix), BioVessel-Net still reached 99.41/99.70, outperforming U-Net++¹⁶ (98.78/99.40), TransUNet²¹ (98.63/99.17), and Tyche⁶⁷ (98.12/99.08). On ROSE, BioVessel-Net kept 99.55/99.78, clearly ahead of other methods such as YOLOv11-x¹¹ (98.72/99.42) and DeepLabV3+⁶³ (98.43/99.21). These results confirm that BioVessel-Net is consistently stronger than CNN baselines (U-Net¹⁵, SegNet⁶²), transformer models (TransUNet²¹, Swin-UNet²⁰), and GAN-based methods (SegAN⁴⁸, Vessel-GAN⁶⁸, CycleGAN-Seg⁷¹).

Table 2. Conducting Mixed Validation on Models using Mixed Datasets ($\times 100\%$)

Model	Dataset															
	ROSE				RetinaMix		OCTA-500		RetinaMix				OCTA-500			
	RetinaMix		OCTA-500		ROSE				6mm		3mm		RetinaMix		OCTA-500	
			3mm													
	IoU	Dice														
U-Net ¹⁵	98.34	99.16	98.32	99.15	93.89	96.85	94.23	97.03	96.21	98.07	95.23	97.56	96.98	98.47	96.81	98.38
U-Net++ ¹⁶	98.99	99.49	98.78	99.39	94.08	96.95	94.46	97.15	95.73	97.82	97.01	98.51	97.59	98.78	96.93	98.44
Attention U-Net ⁴⁹	98.54	99.26	98.23	99.11	94.07	96.94	94.52	97.18	96.99	98.47	96.09	98.01	97.21	98.59	96.78	98.36
Mask R-CNN ¹⁸	96.37	98.15	96.31	98.12	90.73	95.14	91.89	95.77	94.23	97.03	94.11	96.97	96.68	98.31	95.96	97.94
YOLOv11-x ¹¹	98.88	99.44	98.72	99.36	94.11	96.97	94.49	97.17	97.32	98.64	96.54	98.24	96.12	98.02	96.63	98.29
MedSAM ¹⁹	99.04	99.52	<u>98.98</u>	<u>99.49</u>	95.01	97.41	95.42	97.66	97.54	98.75	95.87	97.89	<u>98.23</u>	<u>99.11</u>	97.46	98.72
CauSSL ¹²	96.83	98.38	95.89	97.90	96.98	98.47	97.83	98.88	99.12	99.56	<u>98.79</u>	<u>99.39</u>	94.87	97.33	95.34	97.62
UniverSeg ⁶⁵	98.96	99.48	98.56	99.28	94.23	97.03	94.59	97.24	96.81	98.38	96.32	98.16	97.91	98.96	<u>98.12</u>	<u>99.05</u>
S2VNet ⁶⁶	<u>99.23</u>	<u>99.61</u>	98.79	99.39	93.89	96.85	95.22	97.55	96.95	98.44	95.83	97.87	97.87	98.95	97.87	98.95
Tyche ⁶⁷	98.78	99.38	98.43	99.21	94.22	97.02	94.98	97.46	96.88	98.41	96.11	98.02	97.84	98.94	97.68	98.87
DeepLabV3+ ⁶³	98.72	99.48	98.39	99.40	96.92	98.31	97.46	98.91	97.05	98.47	96.89	98.35	97.62	98.99	96.93	98.28
SegNet ⁶²	98.21	99.12	97.96	99.00	96.41	98.07	97.03	98.64	96.58	98.18	96.23	97.95	97.11	98.72	96.36	97.89
TransUNet ²¹	98.95	99.57	98.66	99.51	97.24	98.66	98.05	99.18	97.63	98.80	97.18	98.62	98.14	99.23	97.26	98.55
Swin-UNet ²⁰	98.98	99.59	98.70	99.53	<u>97.31</u>	<u>98.71</u>	<u>98.09</u>	<u>99.22</u>	97.69	98.84	97.25	98.67	98.18	99.26	97.32	98.59
OCTA-Net ⁷²	99.04	99.62	98.75	99.56	96.98	98.34	97.69	98.83	97.74	98.87	97.31	98.70	98.22	99.29	97.37	98.63
SAM ⁶⁴	98.84	99.51	98.55	99.45	97.10	98.58	97.92	99.10	97.51	98.73	97.05	98.54	97.96	99.14	97.12	98.49
SegAN ⁴⁸	98.43	99.27	98.14	99.18	96.72	98.29	97.55	98.89	97.16	98.52	96.79	98.22	97.61	98.93	96.86	98.17
Vessel-GAN ⁶⁸	98.90	99.54	98.61	99.49	97.20	98.64	98.01	99.16	97.60	98.78	97.15	98.60	98.08	99.20	97.22	98.53
LGGAN ⁶⁹	98.58	99.36	98.29	99.28	96.88	98.40	97.72	98.97	97.30	98.63	96.94	98.36	97.79	99.02	97.02	98.31
CSGAN ⁷⁰	98.63	99.39	98.34	99.32	96.94	98.43	97.77	99.01	97.36	98.66	97.00	98.39	97.83	99.05	97.08	98.34
CycleGAN-Seg ⁷¹	98.69	99.43	98.40	99.36	97.01	98.48	97.84	99.04	97.42	98.70	97.06	98.44	97.90	99.08	97.14	98.38
BioVessel-Net	99.55	99.78	99.21	99.60	97.38	98.76	98.14	99.25	<u>98.87</u>	<u>99.43</u>	98.81	99.40	99.58	99.79	99.41	99.70

Note: the second row corresponds to the model test set, while the third row represents the training set.

Ablation Experiment

Component-Wise Ablation of BioVessel-Net

For baseline GAN model¹³, GAN¹³ and CycleGAN¹⁴ are selected. For baseline segmentor, U-Net¹⁵, U-Net++¹⁶, Attention U-Net¹⁷ and MedSAM¹⁹ are selected. For BioVessel-Net, the different values of R_{min} are tested to evaluate the model segmentation accuracy. As shown in Table 3, since main blood vessels make up a small proportion, the value calculated is also relatively low. When the minimum radius ratio is found, like BioVessel-Net, aligning with biostatistical properties, segmentation accuracy peaks, reinforcing the model's strong clinical interpretability.

Hyperparameter Sensitivity Analysis

As shown in Figure 6, the optimal choice of R_{min} (0.2) enables BioVessel-Net to significantly outperform other models in segmentation, which is so high that it is nearly perfect, approaching 100%. When $R_{min} = 1$, BioVessel-Net segments only the largest vessels, resulting in an extremely low segmentation index as only the starting points meet the threshold. When R_{min} is 0, it is equivalent to no filtering, directly the original image. Also, a greater number of generated nodes N leads to smoother vessel edges, a more complete vascular structure, and improved segmentation accuracy. Given that the R values of BioVessel-Net are relatively low, their practical significance indicates minimal differences in the segmented vessels, as the number of nodes remains similar. Consequently, their curves largely overlap, with BioVessel-Net exhibiting a slight increase.

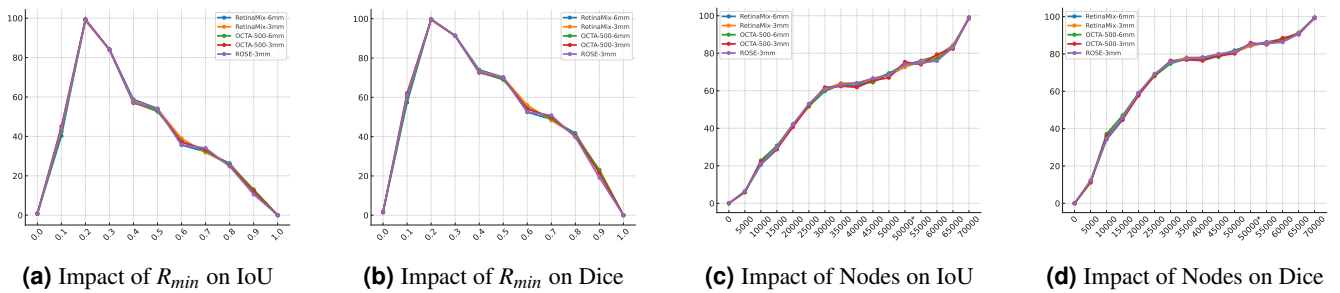


Figure 6. Ablation Experiment of Hyperparameters ($\times 100\%$)

Table 3. Ablation Experiment of BioVessel-Net ($\times 100\%$)

Model		Dataset									
		RetinaMix				OCTA-500				ROSE	
		6mm		3mm		6mm		3mm		3mm	
		IoU	Dice								
GAN ¹³	U-Net ¹⁵	92.89	96.31	92.44	96.07	93.31	96.56	92.84	96.31	93.37	96.59
GAN ¹³	U-Net++ ¹⁶	93.62	96.70	92.87	96.30	93.72	96.73	93.03	96.36	92.84	96.31
GAN ¹³	Attention U-Net ¹⁷	93.56	96.67	93.12	96.44	93.65	96.70	92.85	96.31	93.42	96.61
GAN ¹³	MedSAM ¹⁹	93.73	96.76	92.76	96.24	92.83	96.30	92.47	96.10	93.76	96.75
GAN ¹³	DFS ⁵²	95.81	97.86	95.24	97.56	94.83	97.33	94.87	97.35	94.73	97.27
CycleGAN ¹⁴	U-Net ¹⁵	93.44	96.61	93.42	96.60	94.73	97.26	93.97	96.89	93.76	96.75
CycleGAN ¹⁴	U-Net++ ¹⁶	93.72	96.76	93.62	96.70	94.58	97.18	94.36	97.05	93.19	96.46
CycleGAN ¹⁴	Attention U-Net ¹⁷	93.79	96.80	93.45	96.61	94.59	97.18	94.29	97.01	94.03	96.89
CycleGAN ¹⁴	MedSAM ¹⁹	94.02	96.92	94.37	97.10	93.83	96.72	94.37	97.19	94.18	96.96
CycleGAN ¹⁴	DFS ⁵²	96.23	98.08	96.42	98.18	96.68	98.33	96.27	98.13	95.83	97.84
CycleGAN*	U-Net ¹⁵	94.56	97.20	94.52	97.18	94.86	97.31	94.79	97.27	94.19	96.94
CycleGAN*	U-Net++ ¹⁶	94.98	97.43	94.36	97.10	94.83	97.29	95.09	97.41	94.27	96.98
CycleGAN*	Attention U-Net ¹⁷	95.06	97.47	95.12	97.50	95.07	97.39	94.97	97.33	94.39	97.04
CycleGAN*	MedSAM ¹⁹	95.33	97.61	95.21	97.55	95.36	97.55	95.11	97.41	94.82	97.27
BioVessel-Net		99.41	99.71	98.66	99.33	99.21	99.60	99.42	99.71	99.19	99.59

* means the model has been optimized.

Evaluation of Vessel Structure Refinement

As shown in Table 4, comparison between CycleGAN¹⁴ and CycleGAN (ours revised version) shows a high structural similarity, with SSIM values ranging from 91.01% to 96.04%. CycleGAN (ours) consistently outperforms CycleGAN¹⁴, achieving higher SSIM and lower MSE across all datasets. The small SSIM difference (less than 4.31%) indicates that both models generate highly similar images, but CycleGAN (ours) preserves image structure better and reduces pixel-level errors, making it the superior model.

Table 4. Comparison Vessel Structure Refinement Images with Real OCTA Images ($\times 100\%$)

Model		Dataset									
		RetinaMix				OCTA-500				ROSE	
		6mm		3mm		6mm		3mm		3mm	
		SSIM	MSE	SSIM	MSE	SSIM	MSE	SSIM	MSE	SSIM	MSE
GAN ¹³	91.76	5.69	90.39	4.43	89.69	9.85	91.06	7.36	87.84	8.73	
CycleGAN ¹⁴	93.75	2.36	94.32	2.39	93.56	1.62	94.58	4.46	91.01	3.83	
GAN*	93.62	3.29	93.87	3.79	91.28	6.98	93.19	5.54	91.73	4.18	
CycleGAN*	95.21	1.88	95.89	1.85	94.82	1.73	96.04	3.10	95.32	2.16	

* means the model has been optimized.

Efficiency Evaluation

Assessment of BioVessel-Net in Terms of Efficiency and Explainability

As shown in Table 5, conventional SLSMs and G-AI+SLSMs exhibit strong dependence on GPU resources, extensive manual annotations, and computationally intensive training, while lacking explainability and robustness across 2D and 3D imaging scenarios. In contrast, the proposed DFS algorithm eliminates the need for annotations, training, and GPUs, and offers high interpretability owing to its radius-threshold-driven design, though its applicability to generalization and 3D extension remains limited. BioVessel-Net provides a balanced solution by integrating biostatistical priors with generative modeling: it avoids annotation dependency, achieves partial explainability, and demonstrates strong cross-dataset generalization as well as direct scalability to 3D imaging. These results highlight the complementary advantages of DFS in efficiency and interpretability and of BioVessel-Net in clinical applicability and translational potential.

Table 5. Comparison of Performance Indicators

Indicator	G-AI+SLSMs	SLSMs	BioVessel-Net	DFS (ours)
GPU	✓	✓	✓	×
Annotation	✓/×	✓	×	×
Training	✓	✓	✓	×
Explainability	×	×	✓/×	✓
2D and 3D	×	×	✓	✓
Generalization	✓	×	✓	×

Efficiency Analysis of DFS Compared with SLSMs

Compared to the segmentor, our adjusted DFS offers unmatched advantages, as shown in Table 6. It requires no separate training or labeling, as DFS is a parameter-efficient algorithm. By eliminating manual annotation, it removes subjective bias from doctors. Additionally, its radius-based segmentation avoids pixel mapping errors in SLSMs, such as interference at vessel edges, inaccuracies at junctions, and mask coverage errors. What is more, the key issue is that both SLSMs and G-AI+SLSMs frameworks are susceptible to fitting problems in segmentation tasks. This arises from the training limitations of the SLSMs model and the nature of the data. In contrast, DFS, as an algorithm rather than a model, is unaffected by this issue.

Table 6. Comparison of Performance Details between DFS and SLSMs

Model	Details			
	Inference Time	Parameters	FLOPs	GPU Utilization
U-Net ¹⁵	21ms	31M	98	low
U-Net++ ¹⁶	62ms	76M	304	high
Attention U-Net ¹⁷	83ms	62M	215	slightly high
MedSAM ¹⁹	425ms	109M	1250	extremely high
DFS (CPU)	0.018ms	0M	0.00028	-
DFS (GPU)	≤ 0.01ms	0M	0.00028	extremely low

Visualization

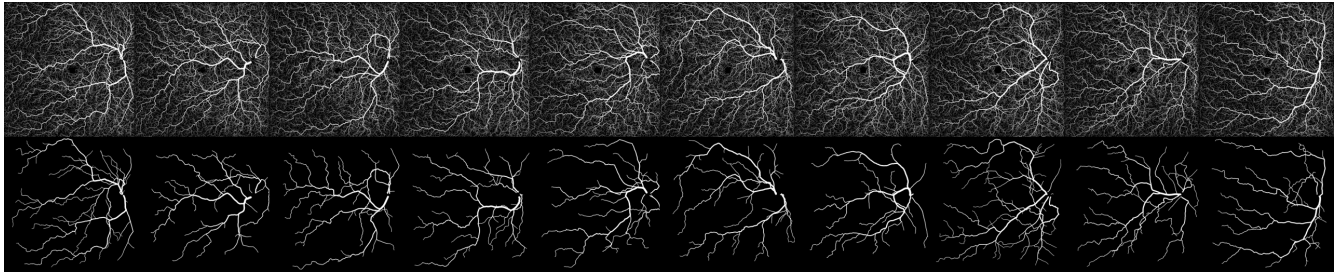
As shown in Figure 7, 2D and 3D segmentation results exhibit smooth, well-defined vessel curves, confirming our prior analysis. In Figure 7a, the segmented vessels are exceptionally smooth, free of pixel artifacts or overflow. DFS effectively filters out vessels below the threshold, eliminating noise and misclassified capillaries. Extending this to 3D, we achieve precise main vessel extraction, with Figure 7e preserving vessel integrity and offering a clearer structure than the original image (Figure 7c).

Analysis

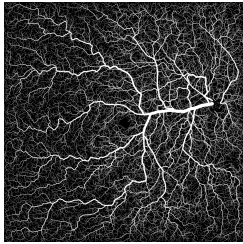
An important aspect of our framework is the selection of the radius threshold R_{min} , which determines the separation between primary vessels and capillaries. Beyond algorithmic considerations, this parameter exhibits clear biological plausibility. Numerous ophthalmology studies have quantified capillary coverage or vessel density across different retinal plexuses using OCTA and histologic imaging. For instance, Lavia et al.^{73,74} reported capillary coverage of approximately 30% in the superficial plexus and 17% in the deep plexus, while Xu et al. (2024)⁷⁵ documented an outer capillary plexus density of $21.9\% \pm 5.9\%$. These values consistently fall within the range of 18–26%, supporting the validity of adopting $R_{min} \approx 0.2$ as a conservative threshold. Thus, the observed robustness of BioVessel-Net is not only algorithmically sound but also biologically interpretable, reflecting established vascular statistics in the ophthalmic literature.

Conclusion

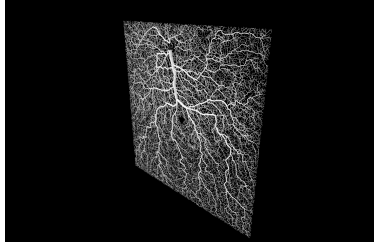
This paper introduced BioVessel-Net, a biologically guided deep learning architecture for accurate segmentation of retinal vessels, and RetinaMix, a high-resolution dataset that provides both two-dimensional and three-dimensional vascular structures with enhanced boundary sharpness and detailed capillary representation. Comprehensive experiments demonstrated that BioVessel-Net achieves state-of-the-art accuracy while preserving anatomical consistency and clinical interpretability. RetinaMix further establishes a superior benchmark for vessel segmentation, enabling rigorous evaluation and fostering future developments in glaucoma-related imaging research. Beyond methodological and dataset contributions, this work highlights the



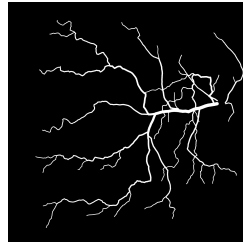
(a) Segmentation of Main Retinal Vessels (2D)



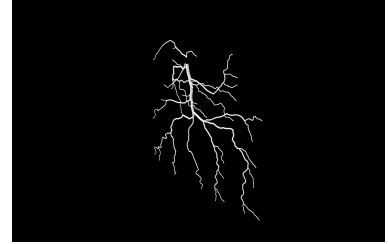
(b) Original Image (2D)



(c) Original Image (3D)



(d) Segmentation (2D)



(e) Segmentation (3D)

Figure 7. Segmentation Results of BioVessel-Net on RetinaMix (2D and 3D)

importance of integrating biological priors into model design and curating datasets that reflect fine-grained vascular morphology. These elements together provide a pathway toward more reliable, interpretable, and clinically relevant tools for glaucoma screening and ophthalmic disease analysis.

Limitation & Future Work

While BioVessel-Net demonstrates near-perfect performance across multiple datasets, several limitations remain. First, our current evaluation focuses on main vessel segmentation; capturing the full capillary network, especially in diseased eyes with irregular morphology, remains highly challenging. Second, although RetinaMix provides a diverse 2D/3D OCTA benchmark, the dataset size is still limited compared to population-scale biobanks, and its generalizability across different imaging devices and clinical settings requires further validation. Third, the biological justification of the radius threshold ($R_{min} \approx 0.2$) is supported by existing ophthalmic studies, yet additional large-scale clinical verification is needed to confirm its universality. Finally, while the unsupervised design reduces dependency on labeled data, full clinical deployment will require integration with diagnostic pipelines and expert-in-the-loop verification.

Future work will extend BioVessel-Net to fine-grained capillary-level analysis, test its robustness on multi-center OCTA cohorts, and explore hybrid frameworks combining unsupervised biostatistical priors with transformer-based architectures for improved scalability. We also plan to release RetinaMix with detailed metadata and baseline benchmarks to facilitate reproducibility and further research in glaucoma imaging.

Acknowledgements

This work was supported in part by the National Natural Science Foundation of China under Grants 62276055 and 62406062, in part by the Sichuan Science and Technology Program under Grant 2023YFG0288, in part by the Natural Science Foundation of Sichuan Province under Grant 2024NSFSC1476, in part by the National Science and Technology Major Project under Grant 2022ZD0116100, in part by the Sichuan Provincial Major Science and Technology Project under Grant 2024ZDZX0012.

Author Contributions Statement

Cheng Huang developed the model and collected the data. Weizheng Xie performed the experimental validation and implemented the analysis scripts. Fan Gao, Yutong Liu, Ruolng Wu, and Hao Wang were responsible for cleaning the raw data. Zeyu Han and Jingxi Qiu set up and tested the model environment. Dr. Xiangxiang Wang, Dr. Yongbin Yu, and Dr. Zhenglin Wang provided funding support and supervised the overall project.

References

1. Tian, Y. *et al.* Fairdomain: Achieving fairness in cross-domain medical image segmentation and classification. In *ECCV*, Lecture Notes in Computer Science (Springer, 2024).
2. Tian, Y. *et al.* Fairseg: A large-scale medical image segmentation dataset for fairness learning using segment anything model with fair error-bound scaling. In *The Twelfth International Conference on Learning Representations*.
3. Huang, C. *et al.* Glaboost: A multimodal structured framework for glaucoma risk stratification. *arXiv preprint arXiv:2508.03750* (2025).
4. Li, M. *et al.* Octa-500: A retinal dataset for optical coherence tomography angiography study. *Med. Image Analysis* **91**, 103016 (2024).
5. Huang, C. *et al.* X-gan: A generative ai-powered unsupervised model for main vessel segmentation of glaucoma screening (2025).
6. Li, L., Xu, M., Wang, X., Jiang, L. & Liu, H. Attention based glaucoma detection: A large-scale database and cnn model. In *Proceedings of the IEEE/CVF Conference on Computer Vision and Pattern Recognition (CVPR)* (2019).
7. Li, L. *et al.* A large-scale database and a cnn model for attention-based glaucoma detection. *IEEE Transactions on Med. Imaging* **39**, 413–424 (2020).
8. Puangarom, S. *et al.* 3-lbnets: Tri-labeling deep convolutional neural network for the automated screening of glaucoma, glaucoma suspect, and no glaucoma in fundus images. In *2023 45th Annual International Conference of the IEEE Engineering in Medicine & Biology Society (EMBC)*, 1–5 (2023).
9. Melo Ferreira, M., Braz Junior, G., Sousa de Almeida, J. D. & Cardoso Paiva, A. Glaucoma grading using multimodal imaging and multilevel cnn. *IEEE Lat. Am. Transactions* **21**, 1095–1102 (2023).
10. d’Ascoli, S. *et al.* Convit: Improving vision transformers with soft convolutional inductive biases. In *Proceedings of the International Conference on Machine Learning (ICML)*, 2286–2296 (2021).
11. Ultralytics. Yolov11: Ultralytics official implementation. <https://github.com/ultralytics/ultralytics> (2024). Accessed: 2025-09-27.
12. Miao, J., Chen, C., Liu, F., Wei, H. & Heng, P.-A. Caussl: Causality-inspired semi-supervised learning for medical image segmentation. In *Proceedings of the IEEE/CVF International Conference on Computer Vision (ICCV)*, 21426–21437 (2023).
13. Goodfellow, I. J. *et al.* Generative adversarial nets. In *Advances in Neural Information Processing Systems (NeurIPS)*, 2672–2680 (2014).
14. Zhu, J.-Y., Park, T., Isola, P. & Efros, A. A. Unpaired image-to-image translation using cycle-consistent adversarial networks. In *Proceedings of the IEEE International Conference on Computer Vision (ICCV)*, 2223–2232 (2017).
15. Ronneberger, O., Fischer, P. & Brox, T. U-net: Convolutional networks for biomedical image segmentation. In *Proceedings of the International Conference on Medical Image Computing and Computer-Assisted Intervention (MICCAI)*, 234–241 (2015).
16. Zhou, Z., Siddiquee, M. M. R., Tajbakhsh, N. & Liang, J. Unet++: A nested u-net architecture for medical image segmentation. In *Proceedings of the International Conference on Medical Image Computing and Computer-Assisted Intervention (MICCAI)*, 3–11 (2018).
17. Oktay, O. *et al.* Attention u-net: Learning where to look for the pancreas. In *Proceedings of the Medical Imaging with Deep Learning (MIDL)* (2018).
18. He, K., Gkioxari, G., Dollár, P. & Girshick, R. Mask r-cnn. *IEEE Transactions on Pattern Analysis Mach. Intell.* **42**, 386–397 (2020).
19. Ma, J. *et al.* Segment anything in medical images. *Nat. Commun.* **15**, 654 (2024).
20. Cao, H. *et al.* Swin-unet: Unet-like pure transformer for medical image segmentation. *Comput. Biol. Medicine* **145**, 105382 (2022).
21. Chen, J. *et al.* Transunet: Transformers make strong encoders for medical image segmentation. In *Proceedings of the International Conference on Medical Image Computing and Computer-Assisted Intervention (MICCAI)*, 485–495 (2021).
22. Huang, C., Yu, A., Wang, Y. & He, H. Skin lesion segmentation based on mask r-cnn. In *2020 International Conference on Virtual Reality and Visualization (ICVRV)*, 63–67 (IEEE, 2020).

23. Huang, C., Yu, Y. & Qi, M. Skin lesion segmentation based on deep learning. In *2020 IEEE 20th International Conference on Communication Technology (ICCT)*, 1360–1364 (IEEE, 2020).
24. Luo, Y. *et al.* Fairclip: Harnessing fairness in vision-language learning. In *Proceedings of the IEEE/CVF Conference on Computer Vision and Pattern Recognition*, 12289–12301 (2024).
25. Luo, Y. *et al.* Fairvision: Equitable deep learning for eye disease screening via fair identity scaling. *arXiv preprint arXiv:2310.02492* (2023).
26. Orlando, J. I. *et al.* Refuge challenge: A unified framework for evaluating automated methods for glaucoma assessment from fundus photographs. *Med. Image Analysis* **59**, 101570 (2020).
27. Fu, H. *et al.* Age challenge: Angle closure glaucoma evaluation in anterior segment oct. *Med. Image Analysis* **59**, 101561, DOI: [10.1016/j.media.2019.101561](https://doi.org/10.1016/j.media.2019.101561) (2019).
28. Iizuka, K., Hoshi, H. & Haga, H. Remodeling mechanisms determine size distributions in vascular trees. *Sci. Reports* **10**, 16888 (2020).
29. Chen, J., Zhang, Y. & Cohen, L. D. Minimal paths for tubular structure segmentation with coherence penalty and adaptive anisotropy. In *Proceedings of the European Conference on Computer Vision (ECCV)*, 710–726 (2018).
30. Nain, D., Yezzi, A. & Turk, G. Vessel segmentation using a shape driven flow. In *International Conference on Medical Image Computing and Computer-Assisted Intervention (MICCAI)*, 51–59 (2004).
31. Huang, C. *et al.* Glalstm: A concurrent lstm stream framework for glaucoma detection via biomarker mining. *arXiv preprint arXiv:2408.15555* (2024).
32. Ma, Y. *et al.* Rose: A retinal oct-angiography vessel segmentation dataset and new model. *IEEE Transactions on Med. Imaging* **40**, 928–939 (2021).
33. Sivaswamy, J., Krishnadas, S. R., Joshi, G. D., Jain, M. & Tabish, A. U. S. Drishti-gs: Retinal image dataset for optic nerve head (onh) segmentation. In *Proceedings of the IEEE International Symposium on Biomedical Imaging (ISBI)*, 53–56 (2015).
34. Zhang, Z. *et al.* Origa-light: An online retinal fundus image database for glaucoma analysis and research. In *Proceedings of the 32nd Annual International Conference of the IEEE Engineering in Medicine and Biology Society (EMBC)*, 3065–3068 (2010).
35. Fumero, F., Alayón, S., Sanchez, J. L., Sigut, J. & Gonzalez-Hernandez, M. Rim-one: An open retinal image database for optic nerve evaluation. In *Proceedings of the 24th International Symposium on Computer-Based Medical Systems (CBMS)*, 1–6 (2011).
36. Foong, A. W. *et al.* Rationale and methodology for a population-based study of eye diseases in malay adults: The singapore malay eye study (simes). *Ophthalmic Epidemiol.* **14**, 25–35 (2007).
37. Diaz-Pinto, A. *et al.* Cnns for automatic glaucoma assessment using fundus images: An extensive validation. *Biomed. Eng. Online* **18**, 29 (2019).
38. Staal, J., Abràmoff, M. D., Niemeijer, M., Viergever, M. A. & van Ginneken, B. Ridge-based vessel segmentation in color images of the retina. *IEEE Transactions on Med. Imaging* **23**, 501–509 (2004).
39. Hoover, A., Kouznetsova, V. & Goldbaum, M. Locating blood vessels in retinal images by piecewise threshold probing of a matched filter response. *IEEE Transactions on Med. Imaging* **19**, 203–210 (2000).
40. Luo, Y., Shi, M., Tian, Y., Elze, T. & Wang, M. Harvard glaucoma detection and progression: A multimodal multitask dataset and generalization-reinforced semi-supervised learning. In *Proceedings of the IEEE/CVF International Conference on Computer Vision*, 20471–20482 (2023).
41. Luo, Y. *et al.* Harvard glaucoma fairness: A retinal nerve disease dataset for fairness learning and fair identity normalization. *IEEE Transactions on Med. Imaging* **43**, 2623–2633 (2024).
42. de Vente, C. *et al.* Airos: Artificial intelligence for robust glaucoma screening challenge. *IEEE Transactions on Med. Imaging* **43**, 542–557 (2024).
43. Kazemina, S. *et al.* Gans for medical image analysis. *Artif. Intell. Medicine* **109**, 101938 (2020).
44. Chen, R. J., Lu, M. Y., Chen, T. Y., Williamson, D. F. & Mahmood, F. Synthetic data in machine learning for medicine and healthcare. *Nat. Biomed. Eng.* **5**, 493–497 (2021).
45. Yoon, J., Jarrett, D. & van der Schaar, M. A review of generative adversarial networks for electronic health records: Applications, evaluation, and challenges. *Proc. IEEE* **108**, 2134–2151 (2020).

46. Toney, A., Reddy, C. K. & Madabhushi, A. Impact of data augmentation and generative modeling on deep learning for medical imaging. *J. Med. Imaging* **8**, 062403 (2021).
47. Bailo, O., Ham, B., Shin, J. Y. & Kim, S. Effects of dataset size and labeling inconsistencies on deep learning for medical image segmentation. *Med. Image Analysis* **58**, 101549 (2019).
48. Xue, Y., Xu, T., Zhang, H., Long, L. R. & Huang, X. Segan: Adversarial network with multi-scale l1 loss for medical image segmentation. In *Proceedings of the International Conference on Medical Image Computing and Computer-Assisted Intervention (MICCAI)*, 690–698 (2018).
49. Vaswani, A. *et al.* Attention is all you need. In *Advances in Neural Information Processing Systems (NeurIPS)*, 5998–6008 (2017).
50. Dosovitskiy, A. *et al.* An image is worth 16x16 words: Transformers for image recognition at scale. In *International Conference on Learning Representations (ICLR)* (2021).
51. Runions, A. *et al.* Modeling trees with a space colonization algorithm. In *Proceedings of the Eurographics Conference on Natural Phenomena*, 63–70 (2007).
52. Cormen, T. H., Leiserson, C. E., Rivest, R. L. & Stein, C. *Introduction to Algorithms* (MIT Press, 2009), 3rd edn.
53. He, K., Sun, J. & Tang, X. Single image haze removal using dark channel prior. In *Proceedings of the IEEE Conference on Computer Vision and Pattern Recognition (CVPR)*, 1956–1963 (2009).
54. Shi, Z., Chen, Y., Gavves, E., Mettes, P. & Snoek, C. G. M. Unsharp mask guided filtering. *IEEE Transactions on Image Process.* **30**, 7472–7485 (2021).
55. He, K., Zhang, X., Ren, S. & Sun, J. Deep residual learning for image recognition. In *Proceedings of the IEEE Conference on Computer Vision and Pattern Recognition (CVPR)*, 770–778 (2016).
56. Isola, P., Zhu, J.-Y., Zhou, T. & Efros, A. A. Image-to-image translation with conditional adversarial networks. In *Proceedings of the IEEE Conference on Computer Vision and Pattern Recognition (CVPR)*, 1125–1134 (2017).
57. Kingma, D. P. & Ba, J. Adam: A method for stochastic optimization. *Int. Conf. on Learn. Represent. (ICLR)* (2015).
58. Everingham, M., Van Gool, L., Williams, C. K. I., Winn, J. & Zisserman, A. The pascal visual object classes (voc) challenge. *Int. J. Comput. Vis.* **88**, 303–338 (2010).
59. Dice, L. R. Measures of the amount of ecologic association between species. *Ecology* **26**, 297–302 (1945).
60. Wang, Z., Bovik, A. C., Sheikh, H. R. & Simoncelli, E. P. Image quality assessment: From error visibility to structural similarity. *IEEE Transactions on Image Process.* **13**, 600–612 (2004).
61. Bovik, A. C. The essential guide to image quality assessment. *Acad. Press. Libr. Signal Process.* **6**, 1–33 (2018).
62. Badrinarayanan, V., Kendall, A. & Cipolla, R. Segnet: A deep convolutional encoder-decoder architecture for image segmentation. *IEEE Transactions on Pattern Analysis Mach. Intell.* **39**, 2481–2495 (2017).
63. Chen, L.-C., Zhu, Y., Papandreou, G., Schroff, F. & Adam, H. Encoder-decoder with atrous separable convolution for semantic image segmentation. In *Proceedings of the European Conference on Computer Vision (ECCV)*, 801–818 (2018).
64. Kirillov, A. *et al.* Segment anything. *arXiv preprint arXiv:2304.02643* (2023).
65. Butoi, V. I. *et al.* Universeg: Universal medical image segmentation. In *Proceedings of the IEEE/CVF International Conference on Computer Vision (ICCV)*, 21381–21394 (2023).
66. Ding, Y., Li, L., Wang, W. & Yang, Y. Clustering propagation for universal medical image segmentation. In *Proceedings of the IEEE/CVF Conference on Computer Vision and Pattern Recognition (CVPR)*, – (2024). Introduces S2VNet.
67. Rakic, M. *et al.* Tyche: Stochastic in-context learning for medical image segmentation. In *Proceedings of the IEEE/CVF Conference on Computer Vision and Pattern Recognition (CVPR)* (2024).
68. Zhou, T., Canu, S. & Ruan, S. Vessel-gan: Retinal vessel segmentation using a generative adversarial network. *Med. Image Analysis* **71**, 102058 (2021).
69. Nie, D. *et al.* Medical image synthesis with context-aware generative adversarial networks. In *Proceedings of the International Conference on Medical Image Computing and Computer-Assisted Intervention (MICCAI)*, 417–425 (2017).
70. Huo, Y. *et al.* Splenomegaly segmentation using global convolutional kernels and conditional generative adversarial networks. In *Proceedings of the International Conference on Medical Image Computing and Computer-Assisted Intervention (MICCAI)*, 174–182 (2018).

71. Huo, Y. *et al.* Synseg-net: Synthetic segmentation without target modality ground truth. *IEEE Transactions on Med. Imaging* **38**, 1016–1025 (2019).
72. Ma, J. *et al.* Octa-net: A retinal vessel segmentation network for optical coherence tomography angiography images. *IEEE Transactions on Med. Imaging* **40**, 2643–2654 (2021).
73. Lavia, C. *et al.* Planimetric quantitative analysis of the retinal microvasculature in healthy subjects by optical coherence tomography angiography. *Retina* **39**, 2477–2485 (2019).
74. Lavia, C. *et al.* Reduced vessel density in the superficial and deep plexuses in diabetic retinopathy is detected by optical coherence tomography angiography. *Ophthalmol. Retin.* **2**, 814–821 (2018).
75. Xu, Y. *et al.* Normative data for retinal vascular density and thickness in a large-scale healthy elderly population assessed by octa. *BMC Ophthalmol.* **24**, 321 (2024).